CFD SIMULATION OF A SUSPENSION MIXING TANK FOR THE PHARMACEUTICAL PROCESSING INDUSTRIES

JIMMY LEA AND JOHN REID
Thales Australia
Garden Island, Sydney, NSW 2011
AUSTRALIA

www.thalesgroup.com

ADESOJI A. ADESINA*
Reactor Engineering and Technology Group
School of Chemical Sciences and Engineering, UNSW, Sydney, NSW 2052
AUSTRALIA

www.reactor.unsw.edu.au

Abstract – The design of suspension mixing tanks is often rooted in empiricism due to inadequate understanding of the hydrodynamics of dense solid-liquid interaction. This is especially limiting during the design of mixing tanks for expensive high quality products in the fine chemicals, biological and pharmaceutical processing industries. In this paper, a CFD-based design methodology has been used to identify six important variables which have significant influence on the ability of a mixing tank to suspend particles. Thus, phenomenologically-rooted correlations between these design variables and key mixing indices – axial mass flow rate in the tank and power consumption were obtained and recommended as objective functions for the optimisation of suspension tank design.

Keywords: CFD, applied mathematics, mixing tank, particles suspension, bioengineering, life sciences

1 Introduction

In the process industry, suspension of particles denser than the fluid media is one of the most common and important objectives. Achieving complete particle suspension leads to homogeneous phase whilst partial particle suspension leads to inhomogeneity and eventually product quality issues. In spite of the industrial relevance of this operation, especially in biochemical manufacturing facilities, the impact on the performance of the suspension mixing tank through changing several crucial variables has received little research attention. Moreover, in many instances the design of a mixing tank for suspending particles is largely based on empirical data. Consequently, operators have to work with sub-optimum process conditions which inevitably lead to poor product quality, consistency and yield. This is particularly germane to the biological and pharmaceutical processing industries where small volume but expensive low volume products is critical to overall plant economics. The pharma sector provides a number of interesting challenges due to the diversity of materials used. Some formulations are extremely viscous and such materials are frequently used for topical application such as creams and ointments. In contrast, other products are required to flow with water-like consistency such as products designed for aural, nasal and ocular administration. In addition, solids loading can be extremely high and a notable case in point is an X-ray contrast media which is 60% (w/w) solid in water. Challenges are set to increase as more bio-pharmaceutical materials, which are anticipated to be shear-sensitive, are brought to market. Despite all these complex and demanding challenges, pharmaceutical mixing is frequently found to be a simple tank and impeller, with design specification focusing on ease with which the vessel can be cleaned and sterilised.

Significant improvements in the design capability and reliability of suspension mixing tank may be expected from advances in computational fluid dynamics (CFD) simulation technology. Hitherto, CFD offers a cost-effective means of capturing the hydrodynamic phenomena and the ability to quantify the performance of a suspension mixing tank.

2 Objectives and KPI

2.1 Objectives

The aim of this paper is to provide a design approach based on the fundamental equations governing the hydrodynamics of multiphase solid-liquid system. This is achievable using computational fluid dynamic investigation of the effect of the key variables on mixing performance.

2.2 Key variables

Six crucial variables known to have a profound effect on the ability of a mixing tank to suspend particles were numerically examined, namely: shaft to impeller diameter (*d/D*), blade width to impeller diameter (*W/D*), impeller to tank diameter (*D/T*), number of blades (N_B), impeller clearance to tank diameter ratio (*C/T*) and impeller rotational speed (*N*). Overall, these six variables constitute the crucial parameters that determine the success of a given geometrical configuration in suspending particles. The geometrical configuration simulated consisted of a standard 6-bladed 45^o pitched-blade turbine, 4 standard wall baffles and a spherical-bottom tank.

2.3 Key Performance Indicator

A horizontal plane across the impeller was created, as shown in Fig. 1, so that surface integration can be conducted to quantify the amount of axial flow passing through the impeller for each trial condition.

Fig. 1 Key performance indicator

Such an approach enables the determination of the axial flow, minus the radial flow component. The amount of axial flow generated is taken as the key performance indicator (KPI). The reason is because it is the axial flow component that pushes the particles to the tank bottom where they are then deflected by the tank bottom causing the particles to travel in the upward direction. In other words, the cloud height is dependent on the amount of axial flow discharge by the impellers [1-2]. A CFD model validation study was successfully carried out via particle image velocimetry (PIV) experiment and the details can be obtained in [3]. The same validated-model was employed for the simulations described in this paper. This ensures the reliability of the models used in this investigation and hence, the integrity of the results presented.

Integrated values were plotted as a function of each variable and the observed relationship modeled by an appropriate mathematical expression. These equations were then employed as objective functions for constrained optimisation.

3 Theoretical consideration

3.1 Meshed geometry

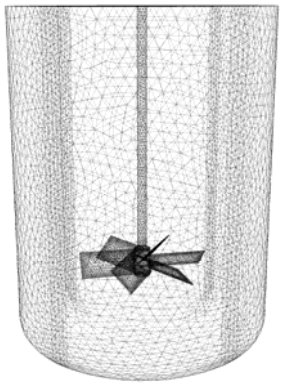

Fig. 2 Key performance indicator

In general, the meshed geometry of the suspension mixing tank was created using Gambit 2.2.30. It consisted of about 473,810 tetrahedral cells, as shown in Fig. 2. A significantly higher number of cells were allocated to area of high velocity and pressure gradient, notably the rotating zones. The baffles were assumed to have zero thickness in order to eliminate additional meshing within the tank. Meshing baffles with non-zero thickness means that very small cells will be required and this can lead to an unnecessarily prohibitive large number of cells with attendant computational costs.

3.2 Grid independence

A preliminary grid convergence study was carried out to verify that the solution obtained from using the second-order upwind discretisation scheme was mesh-independent. The number of cells inside and

outside the rotational zones was systematically increased in the x-, y- and z-directions throughout the tank. When refining the mesh, care was taken to assign additional cells to the regions of high gradient around the impeller blades and discharge regions. Simulation results did not show significant changes (<1%) when the number of cells was increased.

3.3 Numerical setup

Fluent 6.2.16 solver was used to create a numerical solution that matches the governing conservation equations. In this study, the focus was on solving the conservation of mass, momentum and turbulence transport with a view to generating a steady-state 3D hydrodynamics profile. The conservation of mass is given as:

$$\frac{\partial \rho}{\partial t} = -(\nabla \cdot \rho \upsilon) \quad (1)$$

where $\partial\rho/\partial t$ is rate of increase of mass per unit volume and $-(\nabla \cdot \rho\upsilon)$ is the net rate of mass addition per unit volume by convection. The conservation of momentum is given as:

$$\frac{\partial \rho \upsilon}{\partial t} = -(\nabla \cdot \rho\upsilon\upsilon) - \nabla p - (\nabla \cdot \tau) + \rho g \quad (2)$$

where $\partial\rho\upsilon/\partial t$ is rate of increase of momentum per unit volume, $-(\nabla \cdot \rho\upsilon\upsilon)$ is the rate of momentum addition by convection per unit volume, $-\nabla p - (\nabla \cdot \tau)$ is the rate of momentum addition by molecular transport per unit volume and ρg is the external force on fluid per unit volume. For constant ρ and μ, insertion of the Newtonian law of viscosity for τ into (2) leads to:

$$\rho \frac{D\upsilon}{Dt} = -\nabla p + \mu \nabla^2 \upsilon + \rho g \quad (3)$$

Equation (3), commonly known as the Navier-Stokes equation, provides the usual starting point for the analysis of flow processes. The finite volume (FV) method uses the integral form of the conservation of equations as its starting point to ensure global conservation. Differential equation is integrated over the volume of each cell to obtain algebraic equations.

To simulate impeller rotations, separate rotational zones in the immediate vicinity of the impellers were created and a multiple reference frame (MRF) approach was employed. This method involved solving the flow characteristics of the inner region using a rotating framework. These results were then used to provide boundary conditions for the outer region which employs a stationary framework to secure solution to the flow characteristics. The results from the outer region were then re-supplied as boundary conditions for the inner region. This iterative procedure was repeatedly performed until a convergent solution was obtained for both regions.

The segregated-implicit method, where the governing equations were solved sequentially was used. To obtain a higher degree of accuracy, all solutions were obtained via the second-order upwind scheme. In this scheme, higher order accuracy was obtained at the cell surfaces whereby the values at the cell centroid were subjected to multidimensional linear reconstruction using the Taylor series expansion, as shown in (4) and (5).

$$\begin{aligned} f(x) = {} & f(x_0) + \frac{1}{1!} f'(x_0)(x - x_0) \\ & + \frac{1}{2!} f''(x_0)(x - x_0)^2 + \ldots \\ & + \frac{1}{n!} f^n(x_0)(x - x_0)^n + R^{n+1} \end{aligned} \quad (4)$$

where

$$R^{n+1} = \frac{1}{(n+1)!} f^{(n+1)}(\xi)(x - x_0)^{n+1} \quad (5)$$

Due to the presence of baffles, significant interrupted rotational flow existed inside the mixing unit thus creating steep pressure gradient. As a result, PRESTO (pressure staggering option) was employed to compute the pressure value at the cell surface by interpolating the values at the cell centroid. The lack of solid body rotation justifies the use of the Realizable *k-ε* model to capture the hydrodynamic phenomenon. The kinetic energy can be represented by:

$$\begin{aligned} & \frac{\partial}{\partial t}(\rho k) + \frac{\partial}{\partial x_j}(\rho k u_j) = -\frac{\partial}{\partial x_i}\left[(\mu + \frac{u_t}{\sigma_k})\frac{\partial k}{\partial x_j}\right] \\ & + G_k + G_b - \rho\varepsilon - Y_M + S_k \end{aligned} \quad (6)$$

and the dissipation rate is represented by:

$$\frac{\partial}{\partial t}(\rho\varepsilon)+\frac{\partial}{\partial x_j}(\rho\varepsilon u_j)=\frac{\partial}{\partial x_j}\left[(\mu+\frac{u_t}{\sigma_\varepsilon})\frac{\partial\varepsilon}{\partial x_j}\right]+ \rho C_1 S_\varepsilon-\rho C_2\frac{\varepsilon^2}{k+\sqrt{v\varepsilon}}+C_{1\varepsilon}\frac{\varepsilon}{k}C_{3\varepsilon}G_b+S_\varepsilon \quad (7)$$

where

$$C_1=\max\left[0.43,\frac{\eta}{\eta+5}\right] \quad (8)$$

$$\eta=S\frac{k}{\varepsilon} \quad (9)$$

$$S=\sqrt{2S_{ij}S_{ij}} \quad (10)$$

In equations (6) and (7), G_k represents the turbulence kinetic energy generated due to the mean velocity gradients whereas G_b is the turbulence kinetic energy due to buoyancy. Y_M represents the contribution of the fluctuating dilation in compressible turbulence to the overall dissipation rate. C_2 and $C_{1\varepsilon}$ are constants while σ_k and σ_ε are the turbulent Prandtl numbers for k and ε respectively.

3.4 Convergence criteria

Simulations were generally considered converged when the residuals for mass, momentum and turbulence k-ε, fell below 1×10^{-4}. Further checks for convergence were made by creating a monitoring point inside the tank and ensuring that the value monitored remained constant with further iterations. This further helps to ensure results integrity.

4 Results and discussion

4.1 d/D

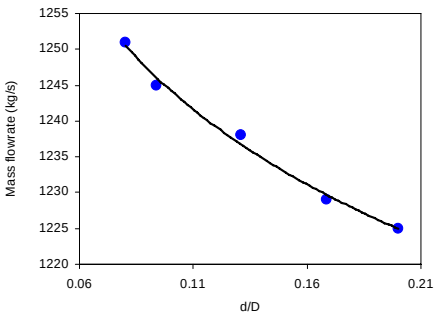

Fig. 3 Mass flowrate vs d/D

Fig. 3 shows a power relationship between the mass flowrate of flow passing through the plane and the shaft diameter to impeller diameter ratio. It is obvious that *d/D* is inversely proportional to the mass flowrate and follows a power function with a good regression of 0.9923, in the form:

$$\dot{m}=1181\left(\frac{d}{D}\right)^{-0.0226} \quad (11)$$

From (11), a 150% increment in *d/D* will reduce the mass flowrate of fluid passing through the plane by 2.0%. That is, a 1% increase in *d/D* will decrease the flowrate by 0.01333%.

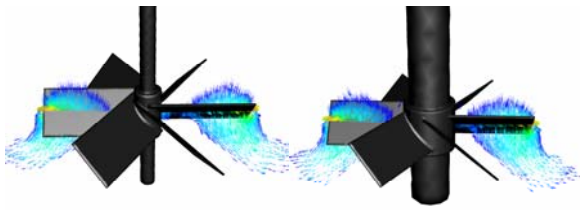

Fig. 4 d/D=0.08 Fig. 5 d/D=0.2

Fig. 4 and 5 show that even though the shaft diameter has been increased by 150%, the flow profile remains the same. The slight reduction in the mass flowrate when the shaft diameter was gradually increased can be attributed to the high flow discharge being located at the blade tip and low flow discharge in the vicinity of the shaft hub.

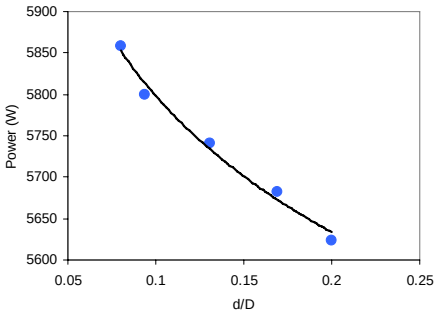

Fig. 6 Power consumed in W vs d/D

Fig. 6 shows that the power consumption in Watts as a function of shaft diameter to impeller diameter ratio follows a power relationship with good regression of 0.9867, in the form:

$$P=5268\left(\frac{d}{D}\right)^{-0.0416} \quad (12)$$

From (12), an increase in the shaft diameter from *d/D*=0.08 to *d/D*=0.2 will reduce the power consumption by only 3.742%. That is, for every

1% increment in *d/D*, the power consumption will reduce by 2.5%. From a practical perspective, it is more beneficial to minimise the shaft diameter without compromising the minimum shaft diameter and maximise the blade length within a given impeller diameter.

4.2 W/D

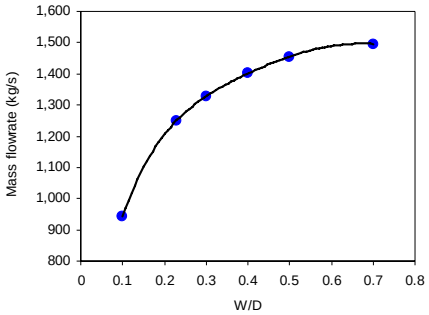

Fig. 7 Mass flowrate vs W/D

Fig. 7 shows the relationship between the mass flowrate and the blade width to impeller diameter ratio. The behaviour can be described by the model:

$$\dot{m} = \frac{a\left(\frac{W}{D}\right)}{1+b\left(\frac{W}{D}\right)} \qquad (13)$$

$\dot{m}$ represents mass flowrate and *W/D* represents the blade width to impeller diameter ratio. Data regression to (13) yielded a=20,000 kg/s and b=12.

When W/D was increased by 200% from W/D=0.1 to W/D=0.3, the increase in flowrate was 43.44%, that is, a 1% increase in W/D increased the flowrate by 0.2172%. When W/D was increased by 25% from W/D=0.4 to W/D=0.5, the increase in flowrate was only 3.595%, that is, a 1% increase in W/D increased the flowrate by 0.1438%.

Beyond this range, the percentage increase in the axial flowrate decreased as the graph levelled. A 400% increase in W/D from W/D=0.5 to W/D=0.7, resulted in an increase of 4.199%, that is, a 1% increase in W/D increased the flowrate by a 0.01050%.

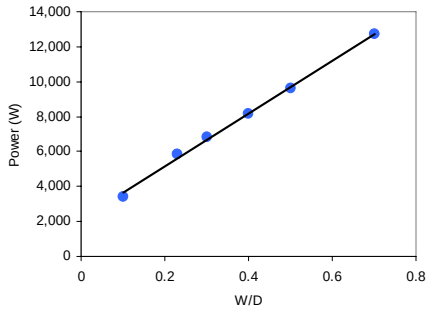

Fig. 8 Power consumed in Watts vs W/D

Fig. 8 shows that the power consumption as a function of the blade width to impeller diameter ratio has a linear relationship, with a good regression of 0.9972. The expression is given by:

$$P = 15162\left(\frac{W}{D}\right) + 2117 \qquad (14)$$

Equation (14) shows that a 1% increase in W/D will increase the power consumption by 0.5890%.

Each time the blades width are increased, there will be an increase in the axial flowrate but beyond W/D=0.3, a higher blade width aspect ratio does not yield any improvement, while below W/D=0.1, the flowrate generated may note be sufficient to suspend the particles. Therefore, from the practical standpoint, it can be seen that for optimum performance, $0.1 \leq W/D \leq 0.3$.

4.3 D/T

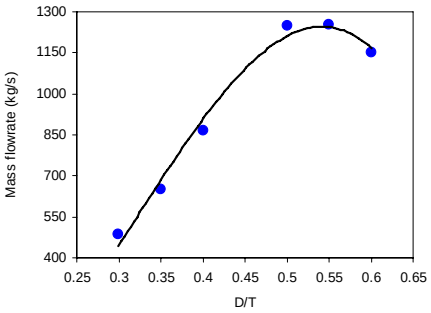

Fig. 9 Mass flowrate vs D/T

Fig. 9 shows the relationship between the mass flowrate and the impeller diameter to tank diameter ratio and is governed by the following third-order polynomial expression,

$$\dot{m} = -31491\left(\frac{D}{T}\right)^3 + 29886\left(\frac{D}{T}\right)^2 - 4648\left(\frac{D}{T}\right) \qquad (15)$$

with a good regression value of 0.9875. Simple differentiation at the turning point shows that the maxima value is located at D/T = 0.54.

From (15), increasing the ratio from D/T=0.3 to D/T=0.54 increased the mass flowrate however, increasing the D/T value beyond the maxima value will cause a reduction in the mass flowrate. From D/T=0.3 to D/T=0.4 (33% increment), the increase in mass flowrate was about 100%, from D/T=0.4 to D/T=0.55 (37.50% increment), the increased was 37.25% and from D/T=0.55 to D/T=0.6 (9.09% increment), the reduction in flowrate was 6.265%. For optimum performance: $0.5 \leq D/T \leq 0.55$.

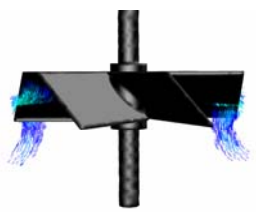

Fig. 10 D/T=0.4

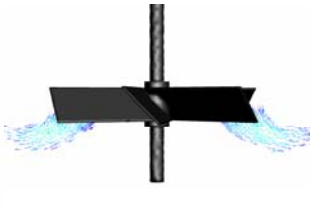

Fig. 11 D/T=0.55

The reason for the reduction in the mass flowrate when the D/T ratio was increased to value beyond the maxima value can be attributed to the change in the flow profile discharged by the impellers. Fig. 10 shows that at D/T=0.4, the flow discharge was axial in nature but when D/T=0.55, the flow changed from axial flow to radial flow as shown by the vector plot in Fig. 11. Obviously, the amount of fluid that passed through the horizontal plane decreased per unit time.

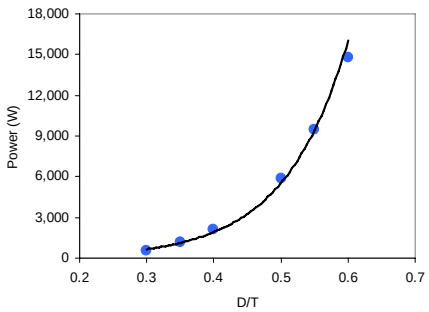

Fig. 12 Power consumed in Watts vs D/T

Fig. 12 shows that the power consumption when D/T was increased from 0.3 to 0.6 follows an exponential relationship with a good correlation coefficient of 0.9956 in the form:

$$P = 27.19e^{10.63\left(\frac{D}{T}\right)} \qquad (16)$$

From (16), when D/T was increased from D/T=0.3 to D/T=0.4, the increased in power consumption was 190%, from D/T=0.4 to D/T=0.55, the increased power consumption was 393% and from D/T=0.55 to D/T=0.6, the increased in power consumption was 70.15%.

The huge increase in the power consumption between D/T=0.4 to D/T=0.55 reflects the high increase in the flowrate. Although the power consumption is higher in this D/T range, it is required to achieve process objective.

4.4 N_B

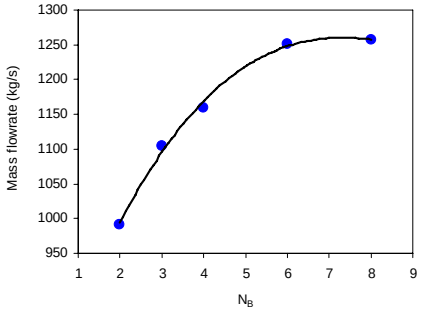

Fig. 13 Mass flowrate vs number of blades

Fig. 13 shows the relationship between the mass flowrate and the impeller diameter to tank diameter ratio and is governed by the following model,

$$\dot{m} = \frac{aN_B}{1+bN_B} \qquad (17)$$

where $\dot{m}$ represents mass flowrate and N_B represents the number of blades. Data regression to (17) yielded a=1667 kg/s and b=1.167 with an excellent correlation fit of 0.9992. The increase in mass flowrate when the number of blades was increased from 2 to 3 blades was 11%, from 3 to 4 blades was 5.851%, from 4 to 6 was 6.287% and from 6 to 8 blades was 3.2%. Increasing the number of blades from 6 to 8 did not return a significantly higher mass flowrate value. From a practical standpoint, a 6-bladed impeller is recommended.

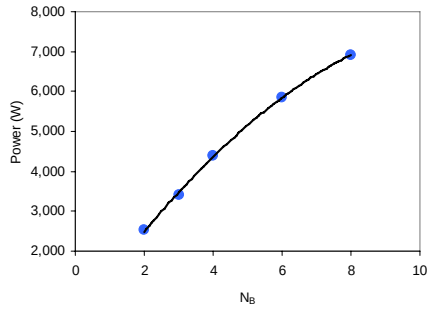

Fig. 14 Power consumed in Watts vs N_B

Fig. 14 shows that the power consumption as a function of the number of blades followed a quadratic polynomial function with a good regression of 0.9994, which can be expressed as:

$$P = -50.07(N_B)^2 + 1241(N_B) + 201.9 \quad (18)$$

Referring to (18), increasing the blades from 4 to 6 will increase the power consumption by 33.91% and 18.48% from 6 to 8 blades.

4.5 C/T

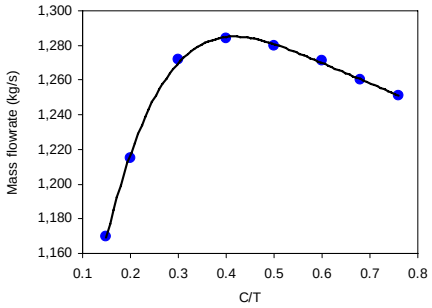

Fig. 15 Mass flowrate vs C/T

Fig. 15 shows the relationship between the mass flowrate and the impeller bottom clearance to tank diameter ratio and is governed by a fourth-order polynomial expression:

$$\dot{m} = \frac{a\left(\frac{C}{T}\right)}{\left[1 + b\left(\frac{C}{T}\right)\right]^2} \quad (19)$$

$\dot{m}$ represents mass flowrate and *C/T* represents the impeller bottom clearance to tank diameter ratio. Data regression to (19) yielded a=13,840 kg/s and b=2.565 with a good correlation fit of 0.9943. For maxima values,

The maxima value is at C/T = 0.3898

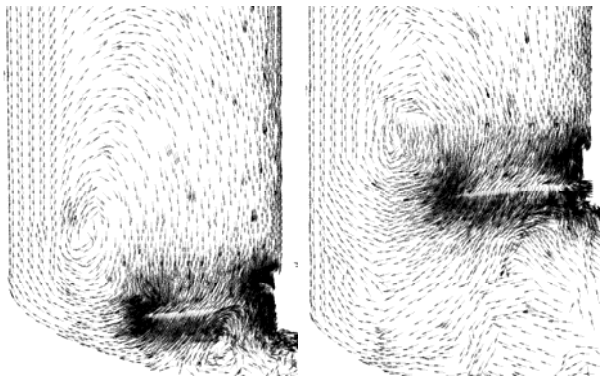

Fig. 16 C/T=0.15 Fig. 17 C/T=0.40

When the impeller was located too close to the tank bottom, for example when C/T=0.15 as shown in Fig. 16, a lower axial flowrate was obtained because of the narrow clearance between the tank bottom and the impeller for the flow to naturally deflect according to the curvature of the tank bottom. The narrow clearance prevented the development of axial discharge from the impellers, forcing the flow discharge to traverse radially. As a result, significant amount of radial flow was produced in place of axial flow. However, when the C/T ratio was increased starting from 0.15 to 0.40 the axial mass flowrate increased by 24.58%. This was because below C/T=0.4, the spherical bottom helped to deflect the axial and radial flow toward the baffles which then directed the flow upward, as shown in Fig. 17. The upward flow at some point re-entered the impeller from the top before emerging from the blade tips. Thus, increasing the amount of fluid moving upwards, through the help of the spherical bottom, will help to discharge higher downward axial flow.

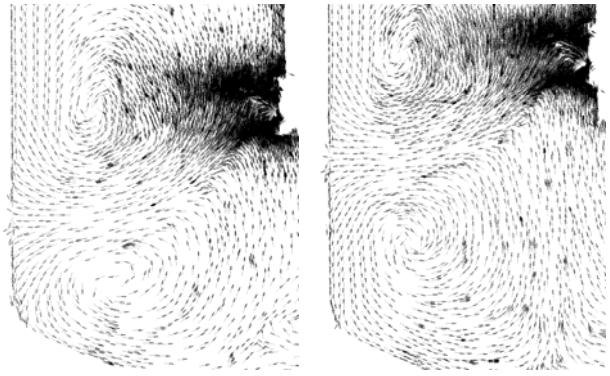

Fig. 18 C/T=0.50 Fig. 19 C/T=0.60

Beyond C/T=0.4, increasing the C/T ratio will cause a decrease in the mass flowrate. Starting from C/T=0.5, a significant component of the flow discharged from the impeller was travelling downward along the wall baffle, as shown in Fig. 18 and Fig. 19. This downward flow was then

directed by the spherical bottom before joining the impeller from the bottom side. This negated the axial flow discharged moving in the downward direction, thus reducing the net axial mass flowrate. The reason was because beyond this maxima value, a major component of the flow discharged came into contact with the baffles first and before being deflected downward. The ideal situation should consist of having the flow discharge coming into contact with the spherical bottom first before being deflected by the baffles upward.

Thus, for optimal performance, $0.15 \le C/T \le 0.4$.

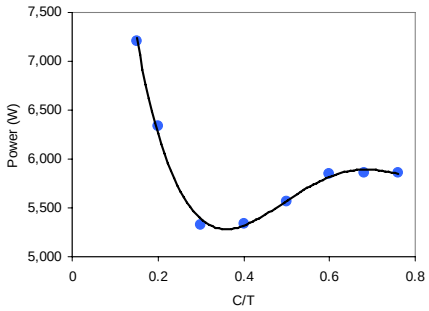

Fig. 20 Power consumed in Watts vs C/T

Fig. 20 shows the power consumed in Watts as a function of impeller clearance to tank diameter ratio can be represented by a fourth-order polynomial expression with a good regression of 0.9959. It can be expressed as:

$$P = 69923\left(\frac{C}{T}\right)^4 - 181238\left(\frac{C}{T}\right)^3 + 165849\left(\frac{C}{T}\right)^2 - 61962\left(\frac{C}{T}\right) + 13375 \quad (20)$$

Minimum power consumption can be obtained at C/T = 0.3593.

Using (20), increasing the C/T ratio from 0.15 to 0.3 will reduce the power consumption rate by 25.57%. Increasing the C/T ratio from 0.4 to 0.6 will cause a 9.423% increment in the power consumed. The reduction in power consumption was due to the lack of interference as the impeller was moved further away from the tank bottom. Beyond the minima point, the power consumption increased again due to the change in the flow pattern where resistant from the baffles was significant.

4.6 N

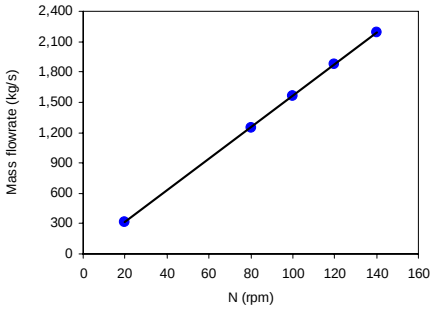

Fig. 21 Mass flowrate vs N

Fig. 21 shows that the flowrate increased by increasing the impeller rotational speed, revealing an excellent linear relationship. It can be expressed as:

$$\dot{m} = 15.65N \quad (21)$$

From (21), an increase in the speed by 1% results in 1% increase in the axial mass flowrate. The recommended impeller rotational speed is any speed that is much greater than the just suspended speed, N_{js}. N_{js} is defined as the minimum rotational speed required to lift the particles from the tank bottom and that no particles remain on the tank bottom for any longer than 1-2 seconds. N_{js} can be obtained via the Zwietering correlation [4], which is given as:

$$N_{js} = S\nu^{0.1}\left[\frac{g(\rho_s - \rho_l)}{\rho_l}\right]^{0.45} X^{0.13} d_p^{0.2} D^{-0.85} \quad (22)$$

where:

S	= Zwietering constant	-
ν	= kinematic viscosity	m^2/s
g	= gravitational constant	m/s^2
ρ_s	= density of solid media	kg/m^3
ρ_l	= density of liquid media	kg/m^3
X	= solid loading	-
d_p	= diameter of solid particles	m
D	= impeller diameter	m

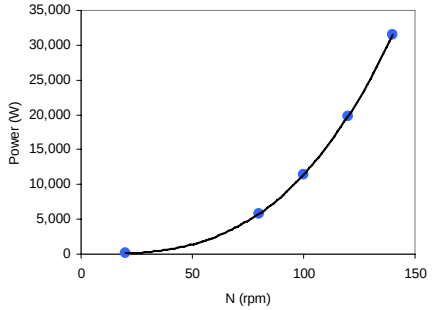

Fig. 22 Power consumed in Watts vs N

Fig. 22 shows that the power consumption relationship with the impeller rotational speed followed a power function with a regression of 1. It can be expressed as:

$$P = 0.0103(N)^{3.0222} \quad (23)$$

Referring to (23), increasing the speed by 300% from 20rpm to 80rpm will increase the power consumption by 5,812%, that is, a 1% increase in the speed in this range will increase the power consumption by 19.37%. Increasing the speed from 80rpm to 140rpm (75%) will increase the power consumption by 442.7%. Therefore for every percent increase in the speed, the power consumed will be increase by 5.902%.

5 Design template

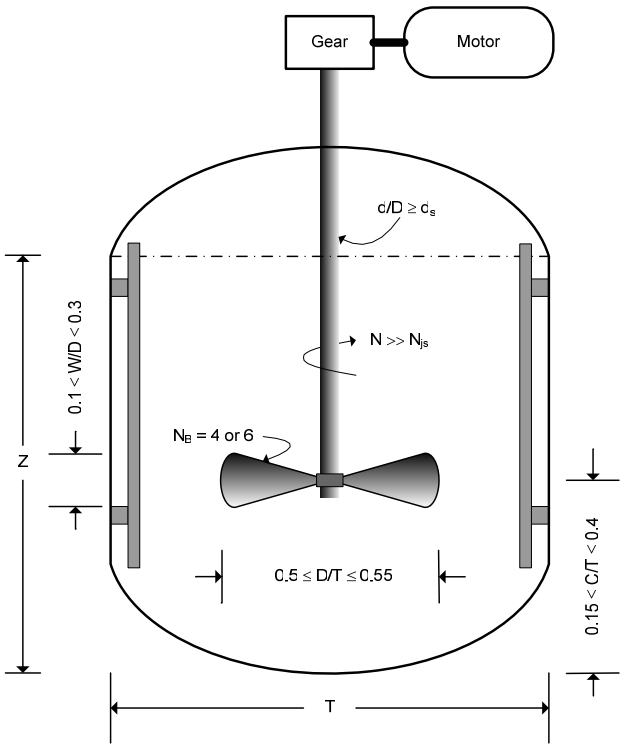

Fig. 23 Design template

The summary of the optimum operating range for each variable can be best represented by a design template shown in Fig. 23, where *Z* and *T* denote liquid height and tank diameter respectively. This template provides a convenient means of optimising a suspension mixing tank without having to conduct time-consuming physical experiments and provides the user a direct route to optimisation. It must be noted however, this design template is only applicable to a contemporary design suspension mixing tank or mixing tank where geometrical configuration resembles that provided in Fig. 23.

6 Conclusion

The behaviour of six variables having profound impact on the ability of a mixing tank to suspend particles has been investigated and was provided in graphical form and mathematical expression. The underlying reasons responsible for the behaviour of each variable under investigation was also provided. Results show that out of the six variables investigated, four variables have an operating range where performance is at its optimum. A design template that summarises the results was provided in this paper as a design guideline.

7 Acknowledgement

The authors are grateful to Mr. Paul Flavel, Manufacturing Operations Manager of Thales Group-Mulwala Plant for encouraging and sponsoring this process R&D project.

References:

[1] Lea J and Adesina A [2006], Simulation of the mixing tank for the production of military high explosive RDX/TNT – A computational fluid dynamics approach, *CHEMECA*, September 17-20 2006, Auckland, New Zealand.

[2] Lea J and Adesina A [2006], Analysis of the mixing tank for cyclotol production: A CFD simulation study, *APCCHE* Aug 27-30 2006, Kuala Lumpur, Malaysia.

[3] Lea J, Gehrig A, Flavel P and Adesina A [2005], The CFD modelling and simulation of nitration unit employed for the manufacture of military propellant, *ICCHMT* May 17-20 2005, Paris, France.

[4] Zwietering T.N. [1958], Suspending of solid particles in liquid by agitators, *Chemical Engineering Science*,Vol 8, 244-253.